



Gap solitons in a one-dimensional driven-dissipative topological lattice

Nicolas Pernet ^{1,5}, Philippe St-Jean ^{1,5}, Dmitry D. Solnyshkov^{2,3}, Guillaume Malpuech², Nicola Carlon Zambon ¹, Quentin Fontaine¹, Bastian Real ⁴, Omar Jamadi⁴, Aristide Lemaître¹, Martina Morassi¹, Luc Le Gratiet¹, Téo Baptiste¹, Abdelmounaim Harouri¹, Isabelle Sagnes ¹, Alberto Amo ⁴, Sylvain Ravets ¹ and Jacqueline Bloch ¹ ✉

Nonlinear topological photonics is an emerging field that aims to extend the fascinating properties of topological states to a regime where interactions between the system constituents cannot be neglected. Interactions can trigger topological phase transitions, induce symmetry protection and robustness properties for the many-body system. Here, we report the nonlinear response of a polariton lattice that implements a driven-dissipative version of the Su-Schrieffer-Heeger model. We first demonstrate the formation of topological gap solitons bifurcating from a linear topological edge state. We then focus on the formation of gap solitons in the bulk of the lattice and show that they exhibit robust nonlinear properties against defects, owing to the underlying sublattice symmetry. Leveraging the driven-dissipative nature of the system, we discover a class of bulk gap solitons with high sublattice polarization. We show that these solitons provide an all-optical way to create a non-trivial interface for Bogoliubov excitations. Our results show that coherent driving can be exploited to stabilize new nonlinear phases and establish dissipatively stabilized solitons as a powerful resource for topological photonics.

The topology of band structures in periodic systems is related to the existence of a non-zero Berry phase, and gives rise to fascinating phenomena like anomalous velocity, chiral edge states (that are robust to disorder) or topological pumps^{1,2}. First discovered in solid-state systems, topological physics can be emulated in artificial lattices including atomic³, photonic^{4,5}, mechanical⁶, optomechanical⁷ and polaritonic^{8,9} systems. These platforms have allowed engineering topological phases hardly achievable in condensed matter, involving synthetic dimensions¹⁰, disorder effects^{11,12}, quasi-crystalline structures¹³ or higher-order multipoles^{14,15}. The physics becomes even richer when interparticle interactions are considered¹⁶. In the weakly interacting regime, nonlinearities induce topological phase transitions^{17–19}, wave mixing among topological modes^{20,21}, enable the formation of solitons in a topological gap^{22–26} or the realization of Thouless pumping with solitons^{27,28}. In the strongly interacting regime, novel symmetry-protected phases may appear²⁹, and fractional quantum Hall physics can be emulated³⁰.

Recently, photonic platforms have allowed pushing this exploration beyond the realm of conservative Hamiltonians, mainly through the engineering of gain and loss. Non-Hermitian topological systems³¹ have led to the development of topological lasing on zero-dimensional^{32–35} or one-dimensional (1D)^{36,37} edge states and PT-symmetric phases^{38,39}. Most of these works on non-Hermitian topology have focused on probing, stabilizing or amplifying the linear response of the system. These recent advances now offer the possibility to experimentally explore topological photonics in a regime where non-Hermiticity and nonlinearity are combined^{39–42}. Driven-dissipative photonic platforms are particularly suited to probe this physics. The external drive can be used to stabilize novel

nonlinear solutions inaccessible to systems subject solely to gain and loss, and to modify the underlying topology⁴³.

In this Article, we investigate the physics of gap solitons in a 1D driven-dissipative topological lattice. We emulate a nonlinear version of the Su-Schrieffer-Heeger (SSH) model: a 1D bipartite topological lattice with staggered hopping energies forming a chain of coupled dimers⁴⁴. Cavity polaritons enable exploring this nonlinear topological physics^{8,9,33,45–47}. Indeed, their excitonic fraction provides repulsive interactions, resulting in a Kerr-type nonlinearity, whereas their photonic component makes the system intrinsically non-Hermitian via loss and possibly gain. Moreover, the system can be resonantly driven and reach a steady state determined by the balance between drive, dissipation and nonlinearity⁴⁸.

We demonstrate the formation of gap solitons that bifurcate either from a topological interface state or from dimers in the lattice bulk. When excited within the topological gap, the solitons present tails that are highly sublattice polarized. This endows them with robustness properties that we probe using an optically controlled non-Hermitian defect (a local complex term perturbing the potential landscape). We demonstrate that these solitons are robust to defects located on one sublattice, a property inherited from the chiral symmetry of the model. The crucial asset of driven-dissipative systems appears when engineering the driving field. By imposing a phase frustration between the driving field and Bloch eigenstates, we demonstrate the generation of gap solitons that have no counterpart in conservative systems and show high sublattice polarization in the core. Crucially, we show how the modification of the potential landscape induced by these asymmetric solitons can effectively split the chain and form a non-trivial interface. This aspect is evidenced through the emergence of a topological edge state in the calculated Bogoliubov excitation spectrum.

¹Université Paris-Saclay, CNRS, Centre de Nanosciences et de Nanotechnologies (C2N), Palaiseau, France. ²Institut Pascal, PHOTON-N2, Université Clermont Auvergne, CNRS, SIGMA Clermont, Clermont-Ferrand, France. ³Institut Universitaire de France (IUF), Paris, France. ⁴Université de Lille, CNRS, Laboratoire de Physique des Lasers Atomes et Molécules (PhLAM), Lille, France. ⁵These authors contributed equally: N. Pernet, P. St-Jean. ✉e-mail: jacqueline.bloch@c2n.upsaclay.fr

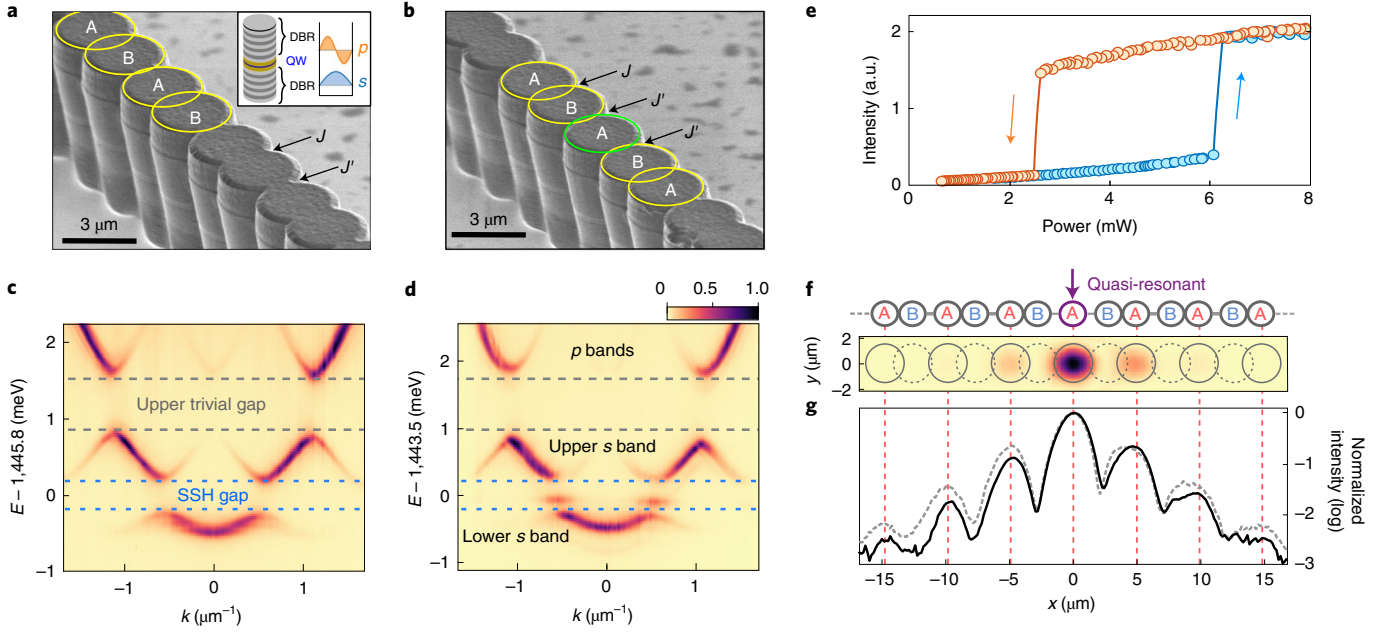


Fig. 1 | Implementation of the SSH lattice. **a,b**, Scanning electron microscopy images of the bulk SSH polariton lattices. We highlight some of the micropillars with yellow circles and an interface defect in **b** with a green circle. Inset of **a**: schematic representation of a micropillar, composed of a Fabry–Perot cavity defined by two distributed Bragg reflectors (DBRs) and a spacer (orange layer) embedding a single quantum well (QW). Right: Typical shape of the *s* and *p* polariton modes. **c,d**, Spectrally resolved photoluminescence intensity measured as a function of momentum *k* under non-resonant excitation using an elongated spot centred in the bulk (**c**) and on the interface defect of the lattice (**d**). **e**, Transmitted intensity measured as the excitation power is ramped up (blue circles) or down (red circles) under quasi-resonant excitation of the interface defect. **f**, Two-dimensional real-space image of the transmitted intensity measured on the topological soliton. The excitation pump is localized on the interface state, as sketched on top of the panel. **g**, Normalized intensity profiles (integrated over the transverse direction) measured for the topological interface state in the linear regime (dashed grey line) and for a topological gap soliton bifurcating from the interface state (black solid line).

Nonlinear driven-dissipative SSH model

The physics of the polariton nonlinear SSH model can be captured by a discretized Gross–Pitaevskii equation including drive and dissipation:

$$i\hbar \frac{d}{dt} \begin{bmatrix} a_n \\ b_n \end{bmatrix} = (E_0 - i\frac{\gamma}{2}) \begin{bmatrix} a_n \\ b_n \end{bmatrix} + g \begin{bmatrix} |a_n|^2 a_n \\ |b_n|^2 b_n \end{bmatrix} - J \begin{bmatrix} b_n \\ a_n \end{bmatrix} - J' \begin{bmatrix} b_{n-1} \\ a_{n+1} \end{bmatrix} + i \begin{bmatrix} F_{a,n} \\ F_{b,n} \end{bmatrix} e^{i\omega t}, \quad (1)$$

where $\Psi_n(t) = [a_n(t); b_n(t)]^T$ is the time-dependent wavefunction spinor on site A and B in the *n*th unit cell, \hbar is the reduced Planck constant, E_0 is the on-site energy, γ is the polariton linewidth, g is the interaction energy, J (J') is the intracell (intercell) coupling energy and $\omega/(2\pi)$ is the driving field frequency setting the polariton field frequency. The driving field $\mathbf{F}_n = [F_{a,n}; F_{b,n}]^T$ can be engineered with a specific amplitude and phase on each site, namely, $F_{\alpha,n} = |F_{\alpha,n}| e^{i\varphi_{\alpha,n}}$.

The topological nature of the SSH model is related to chiral (or sublattice) symmetry. Zero-energy states, which emerge in lattices ending with weak links, are protected by this symmetry. They are localized on a single sublattice, thus presenting well-defined sublattice pseudospin:

$$\tilde{S} = \frac{\sum_n |a_n|^2 - |b_n|^2}{\sum_n |a_n|^2 + |b_n|^2} = \pm 1. \quad (2)$$

The sign of the spin reflects the sublattice localization, either on A (+1) or B (−1). The existence of topological edge states can be related to the winding number \mathcal{W} computed over the first

Brillouin zone⁴⁹ that can take the values of 0 (strong-link termination) or 1 (weak-link termination). Hereafter, we will show that the specific properties of gap solitons generated in the nonlinear driven-dissipative SSH model are linked to the pseudospin evaluated in their core and in their exponential tails.

To emulate this system with cavity polaritons, we design arrays of coupled micropillars (3.0 μm diameter), with alternating short (2.2 μm) and long (2.75 μm) centre-to-centre distances (Fig. 1a). At the centre of some lattices, we create an interface defect by inserting a pillar surrounded by two consecutive long centre-to-centre distances (Fig. 1b). These arrays are fabricated by etching a planar cavity containing a quantum well (Methods).

The linear spectrum of these structures is probed by low-temperature (4 K) photoluminescence experiments (Methods). Imaging the emission with angular resolution enables observing polaritonic bands in momentum space (Fig. 1c,d and Supplementary Section 1). Real-space images are shown in Supplementary Section 2. The two lowest-energy bands originate from the hybridization of the lowest-energy mode (*s* mode) of each pillar and emulate the single-particle SSH model with a 0.45 meV topological gap. The spectrum asymmetry with respect to the centre of this gap is attributed to couplings between the *s* modes and the next modes of higher energy (*p* modes)⁵⁰. Interestingly, when the excitation overlaps an interface defect (Fig. 1d), a topological state localized on the interface pillar is observed in the topological gap (Supplementary Fig. 2).

Focusing the pump on the interface, we first evidence a topological soliton that bifurcates from a linear topological state. We tune the laser energy to 180 μeV (approximately 2.5γ) above the topological interface state and measure the transmitted signal when scanning the excitation power up and down. As shown in Fig. 1e, a hysteresis cycle is observed in the transmitted intensity, as expected in the

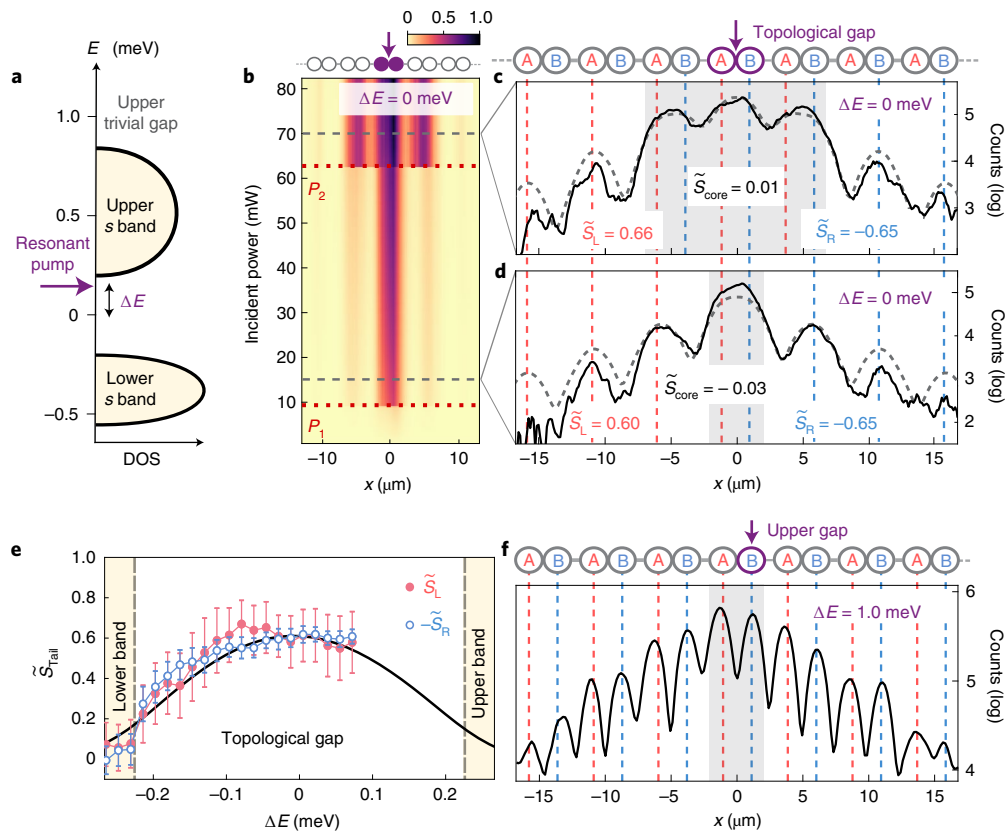


Fig. 2 | Generation of topological gap solitons. **a**, Spectral density of states (DOS) of the SSH lattice. The drive (purple arrow) is detuned from the centre of the topological gap by ΔE . **b**, Spatially resolved intensity (integrated over the direction perpendicular to the lattice and normalized to their maximum value), measured as we ramp up the driving power. The dotted horizontal red lines mark the P_1 and P_2 thresholds. **c,d**, Experimental (solid line) and simulated (dashed line) spatial profiles of the soliton above P_2 (**c**) and P_1 (**d**) thresholds (the corresponding excitation powers are indicated with dotted black lines in **b**). **e**, Pseudospins \tilde{S}_L (red full circles) and $-\tilde{S}_R$ (blue open circles) measured as a function of ΔE . The amount of optical power available in the experiment enables exploring positive ΔE values up to 0.1 meV only. The error bars are calculated by evaluating the impact of the area chosen for intensity integration on the result. The grey solid line shows the values of \tilde{S}_L obtained using a tight-binding calculation, where the intensity on each site is convoluted with a Gaussian profile with FWHM of $2.7 \mu\text{m}$ (about the FWHM of the s mode of the pillar). **f**, Soliton profile measured when the laser energy is tuned to the upper trivial gap ($\Delta E = 1.0 \text{ meV}$). In **b-d** and **f**, the location of the drive is indicated with a purple arrow in the sketch above. In **c, d** and **f**, the red (blue) dashed lines indicate the A (B) sites with peaked intensity whereas the grey areas represent the extent of the soliton cores.

presence of Kerr nonlinearities. The high-intensity branch manifests the generation of a gap soliton. It presents the same spatial profile as the linear topological interface state (Fig. 1f,g): a core self-localized at the defect position surrounded by two sublattice-polarized exponentially decaying tails.

Bulk gap solitons

We now address the nonlinear response in the bulk of the SSH lattice (Fig. 1a). We implement a quasi-resonant excitation scheme using a laser spectrally detuned by $\Delta E = \hbar\omega - E_0$ with respect to the centre of the topological gap at energy E_0 (Fig. 2a). We focus the laser (full-width at half-maximum (FWHM), $3.5 \mu\text{m}$) ten unit cells away from the lattice edges to avoid finite size effects, and measure the transmitted intensity.

We first consider an excitation scheme where the pump frequency is tuned to the centre of the topological gap ($\Delta E = 0$) and the beam is focused onto the centre of a dimer. This corresponds, in equation (1), to a driving field localized on a single dimer with equal amplitude and phase on both A and B sites. By ramping up the driving power, we observe the formation of gap solitons that are symmetric with respect to the pump and localized on a discrete number of dimers (Fig. 2b). When the incident power reaches the first threshold (denoted by P_1), we observe the formation of a bulk

soliton with a core extending over one dimer. Above threshold P_2 , the soliton core extends to three dimers. Looking at the total transmitted intensity when scanning the power up and down, we evidence bistability and hysteretic behaviour at each nonlinear threshold (Supplementary Section 3). Each threshold occurs when the nonlinear blueshift induced by the polariton interaction energy within a dimer overcomes the spectral detuning between the pump and the top of the lower band. These solitons are composed of a self-localized core region (Fig. 2c,d, grey-shaded areas) and of exponentially decaying tails on both sides. Due to the lattice inversion symmetry, the soliton pseudospin computed over the entire profile vanishes⁵¹: $\tilde{S}_{\text{tot}} = -0.10 \pm 0.06$ after P_1 and $\tilde{S}_{\text{tot}} = 0.09 \pm 0.04$ after P_2 . Note that variations in P_1 are observed when pumping different dimers. They are due to disorder-induced on-site energy fluctuations of about $15 \mu\text{eV}$. These are smaller than the polariton linewidth ($\gamma \approx 70 \mu\text{eV}$) and do not influence the physics discussed here.

It is insightful to probe how the pseudospin varies over the profile. Inside the soliton core, each dimer shows similar amplitude on both sublattices, leading to a locally vanishing pseudospin⁵¹: $\tilde{S}_{\text{core}} = -0.03 \pm 0.09$ after P_1 and $\tilde{S}_{\text{core}} = 0.01 \pm 0.06$ after P_2 (Fig. 2c,d). In contrast, the evanescent tails are strongly localized on a single sublattice: the A sublattice on the left and the B sublattice on the right. Consequently, the pseudospins \tilde{S}_L and \tilde{S}_R integrated over the

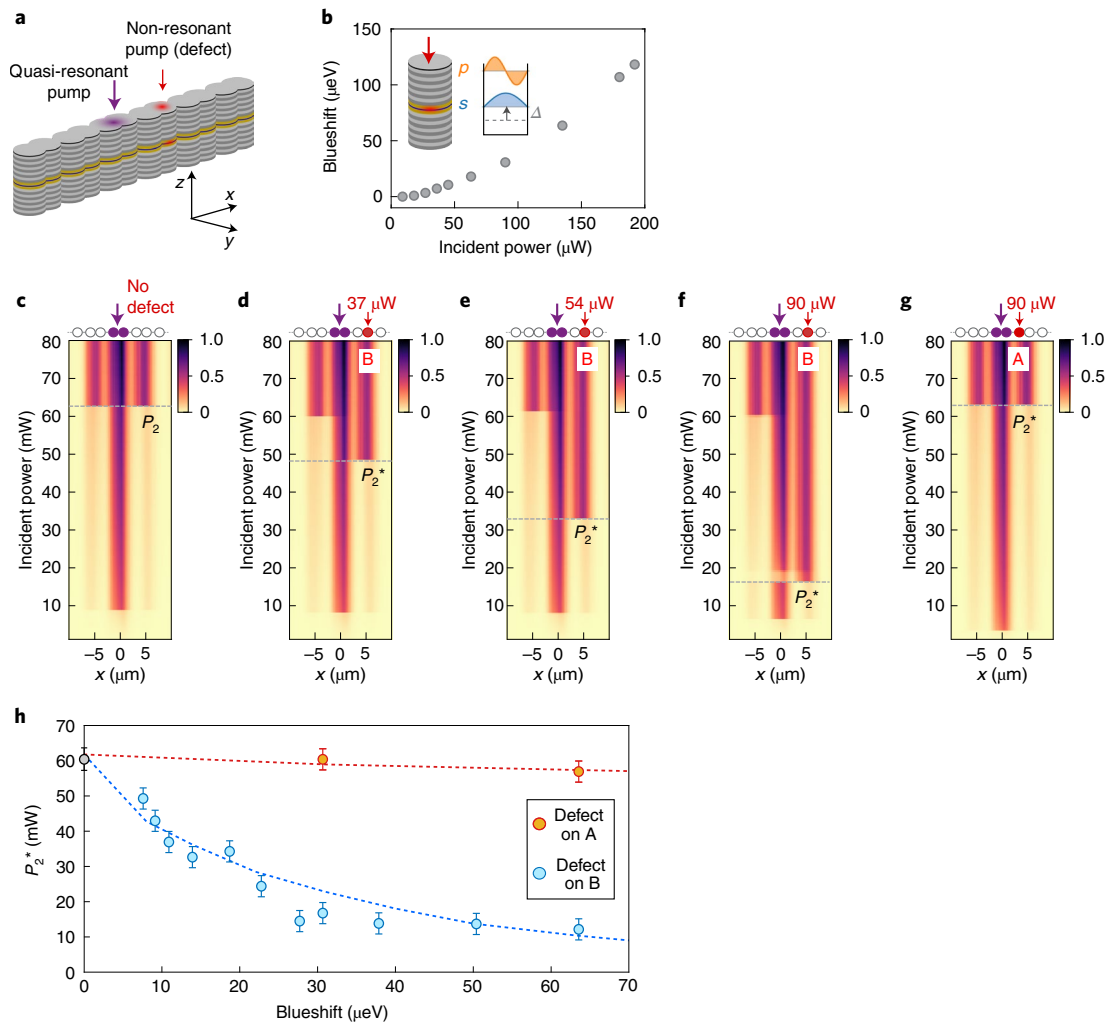


Fig. 3 | Robustness of gap solitons against a defect. **a**, Schematic of the two-beam experiment to generate both soliton (quasi-resonant pump; purple arrow) and optically induced defect (non-resonant pump; red arrow). **b**, Calibration of the optical defect: blueshift Δ as a function of the non-resonant pump power measured on the calibration micropillar. **c–g**, Spatially resolved intensity profiles (integrated along the direction perpendicular to the lattice and normalized to their maximum value), measured as we ramp up the driving power for no defect (**c**), a defect on the B sublattice generated with various non-resonant powers (**d–f**) and a defect on the A sublattice (**g**) generated with the same power as in **f**. For each panel, the driven dimer (defect) is shown on top with purple (red) circles. **h**, Threshold power P_2^* measured as a function of the blueshift (deduced from **b**) induced by a defect localized on the A (red symbols) or B (blue symbols) sublattice. The red and blue lines correspond to numerical simulations. The error bars correspond to the standard deviation on the measurement of P_2 obtained by performing a repeatability study on the resonant pump alignment.

left and right soliton tails are non-zero and present opposite signs: $\tilde{S}_L > 0$ and $\tilde{S}_R < 0$ (Fig. 2c,d).

The spin of the bulk soliton tails can be further explored when varying the laser energy. In Fig. 2e, we report the measured \tilde{S}_L and \tilde{S}_R when varying ΔE within the topological gap. The spin polarization of the tails reaches its maximum close to the centre of the gap and decreases when approaching the bands (Supplementary Section 4 provides the measured profiles). We now compare these features with the case of solitons generated in the gap separating the s and p bands. To do so, we tune the laser energy to the upper gap and focus the laser spot onto a single site to efficiently couple to the upper SSH band (anti-bonding symmetry). The soliton profile obtained when exciting this trivial gap is presented in Fig. 2f. Both evanescent tails present high intensities on all pillars and thus show no spin polarization.

To accurately reproduce the experimental data, we use an effective 1D continuous model, which allows to take into account the finite size of the lattice pillars and the mixing of s – p bands.

We look for steady-state solutions of a 1D driven-dissipative Gross–Pitaevskii equation. The strong and weak links are represented by barriers in the potential (Supplementary Section 5). Numerical results shown in Fig. 2c,d (and Supplementary Fig. 6) reproduce the measured soliton profiles with their characteristic tails of opposite spin polarization.

Robustness of bulk gap solitons to non-Hermitian defects

In conservative SSH lattices, theoretical calculations predict the interaction of gap solitons with a defect to be strongly influenced by the spin polarization of their tails²³. Hereafter, we extend this idea to the driven-dissipative framework, and show that the nonlinear threshold for the lateral growth of the soliton core is immune to the presence of a defect on one sublattice but not on the other.

We monitor how the spatial expansion of the soliton core is affected by a defect positioned on a pillar belonging to a neighbouring dimer. The defect is optically generated by non-resonantly pumping a pillar belonging to the A or B sublattice with a second

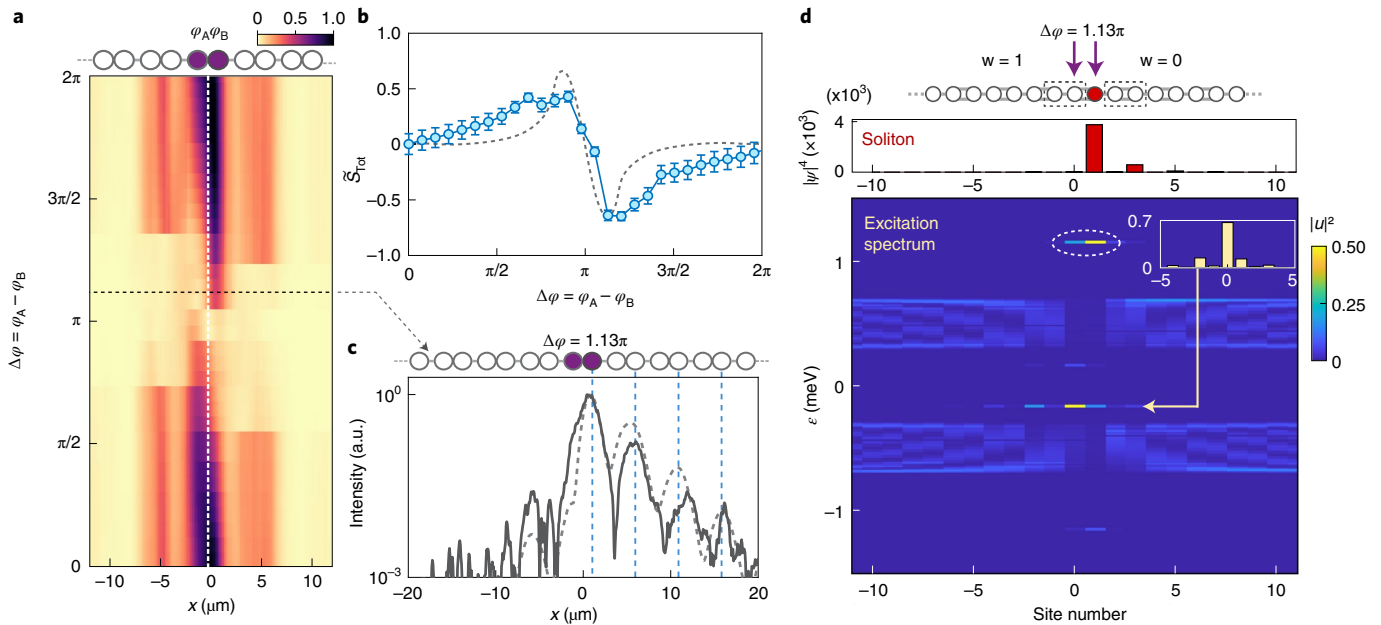


Fig. 4 | Spin-polarized solitons. **a**, Spatially resolved intensity (integrated along the direction perpendicular to the lattice and normalized to their maximum value), measured as a function of $\Delta\varphi$ for a total excitation power $P = 80 \text{ mW}$ ($P > P_2$). The driven dimer is indicated on the top (purple discs). The white vertical dashed line indicates the centre of the driven dimer. **b**, Measured (symbols) and calculated (dashed line) soliton total pseudospin \tilde{S}_{tot} , as a function of $\Delta\varphi$. The error bars are calculated by evaluating the impact of the area chosen for intensity integration. **c**, The intensity profile of the soliton measured (solid line) and simulated (dashed line) for a phase difference $\Delta\varphi = 1.13\pi$ (indicated by the horizontal dashed line in **a**). The blue dashed lines mark the B pillars with peaked intensity. **d**, Calculated Bogoliubov excitation spectrum (bottom) when driving a dimer with $\Delta E = 0$, $\Delta\varphi = 1.13\pi$ and an excitation power corresponding to the maximum spin polarization of the soliton core. The white dashed ellipse highlights the blueshifted site, and the arrow points towards the mode emerging in the gap (the mode profile is shown in the inset). Above the Bogoliubov spectrum, we show the intensity profile of the bulk soliton (red bars). The top shows an illustrative schematic depicting the chain. The red disc shows the site where the eigenmode has effectively been decoupled from the bands. The white discs illustrate the two remaining semi-infinite chains together with their winding numbers \mathcal{W} , determined from the coupling strength at their termination.

laser (Fig. 3a). This creates a local reservoir of excitons whose effect is twofold: (1) it locally blueshifts the pillar on-site energy (perturbation on the real part of the potential); (2) it induces a local gain through the stimulated relaxation of excitons towards polariton modes (perturbation of the imaginary part of the potential). This defect is, therefore, intrinsically non-Hermitian.

To calibrate the real part of this perturbation, we measure the spectral shift of the ground state from a single micropillar with similar characteristics as those forming the chain (Fig. 3b). The imaginary part (gain) is deduced from the lasing threshold ($P_{\text{th}} \approx 0.6 \text{ mW}$) in the calibration pillar (Supplementary Section 7).

The evolution of the spatial profile of the soliton as we ramp up the resonant pump power is displayed in Fig. 3d–g for different amplitudes and positions of the defect. For comparison, the case without a defect is shown in Fig. 3c. We first monitor the soliton-core expansion in the presence of a defect located on the B sublattice, where the soliton-tail intensity presents local maxima (Fig. 3d–f and Supplementary Section 7). As the defect breaks the spatial symmetry of the system and locally reduces the laser detuning, the soliton-core expansion becomes asymmetric. It is favoured towards the defect at power P_2^* . At higher power, close to power P_2 measured without a defect, the soliton eventually recovers a symmetric profile. We observe in Fig. 3h that P_2^* strongly varies with the defect amplitude. The simulations shown in Fig. 3h reproduce this behaviour when including the calibrated values of both real and imaginary parts of the perturbation (Supplementary Section 7 and Supplementary Fig. 8).

This observation contrasts with what we measure when localizing the defect on the A sublattice, where the amplitude of the tails vanishes. In that case, the second nonlinear expansion simultaneously

occurs toward the right and left dimers, regardless of the defect amplitude (Fig. 3g,h) and for a power close to P_2 measured without defect. This demonstrates that solitons in the topological gap present high robustness against non-Hermitian defects located on one sublattice because of the spin polarization of their tails. This would also apply to the topological solitons discussed earlier, which bifurcate from a topological edge state. Moreover, as discussed elsewhere³³, linear topological edge states at zero energy are immune to disorder in the coupling constants of the SSH lattice, as long as the topological gap remains open. These properties still hold for the gap solitons discussed here.

Spin-polarized gap solitons using phase-engineered drive

The bulk gap solitons considered so far present a globally vanishing pseudospin, like in conservative systems⁵¹. Hereafter, we show how we can depart from this family of unpolarized solutions owing to the driven-dissipative nature of polaritons. To do this, we turn to an excitation scheme where two pillars of a dimer are driven with two beams with the same amplitude and tunable phase difference $\Delta\varphi = \varphi_A - \varphi_B$ (Fig. 4a). In equation (1), this corresponds to a driving field localized on a single dimer with equal amplitude on both sublattices, but different phases. We select a total excitation power $P > P_2$ to obtain a three-dimer soliton when $\Delta\varphi = 0$. Figure 4a presents the evolution of the intensity distribution along the lattice on increasing $\Delta\varphi$. A sequence of abrupt switchings is revealed between distinct regimes where the soliton core changes size. Close to $\Delta\varphi = \pi$, the driving field becomes orthogonal to the lower-band Bloch modes, strongly reducing light injection and explaining the switching to the linear regime.

For non-zero values of $\Delta\varphi$, the soliton exhibits a non-zero total sublattice polarization, which reaches a maximum close to $|\tilde{S}_{\text{Tot}}|=0.5$ in the vicinity of $\Delta\varphi=\pi$ (Fig. 4b). Remarkably, the soliton core is then localized on a single site of the driven dimer, whereas the other driven site experiences a destructive interference induced by the nonlinearity. We show (Fig. 4c) the experimental and theoretical spatial profiles of this soliton for $\Delta\varphi=1.13\pi$. As can be analytically derived (Supplementary Section 9), when assuming perfect destructive interference in one of the two sites of the driven dimer, the resulting profile is found to be the same as that of an SSH topological edge state. We emphasize that the novel family of spin-polarized gap solitons reported here does not exist in conservative or undriven systems, as a phase-patterned driving field is required to stabilize them (Supplementary Section 8).

Highly spin-polarized gap solitons have striking consequences on the physics of the underlying excitations. These consequences are related to the nonlinear on-site energy blueshifts locally induced by solitons. For $\Delta\varphi=1.13\pi$, the soliton core creates a local potential barrier strongly localized on a single site and effectively splits the lattice in two semi-infinite SSH chains, one of them showing a weak-link termination ($\mathcal{W}=1$). This suggests the optical creation of a non-trivial interface. For a more quantitative analysis of this effect, we compute the Bogoliubov spectrum of the system (Methods), in the presence of a spin-polarized soliton. We consider a situation similar to the experiment, where the soliton is generated at energy $\Delta E=0$ using two pumps localized on sites 0 and 1 and $\Delta\varphi=1.13\pi$. The spatial profile of the soliton (obtained for the drive power corresponding to optimal destructive interference within the driven dimer) is shown in the top part of Fig. 4d, and the spatial profile of the Bogoliubov modes is shown in the bottom. The Bogoliubov spectrum clearly shows a high-energy mode strongly localized at the soliton core position on site 1 (white dashed ellipse), which is a signature of the large blueshift experienced by this site. The vanishing amplitude of the Bloch band states at this position suggests that the lattice has effectively been split into two parts. Remarkably, we observe the emergence of a Bogoliubov mode within the topological gap (Fig. 4d, arrow), together with its particle–hole symmetry with respect to the pump energy $\varepsilon=0$ (ref. 52). This mode is localized on site 0 (weak-link termination with $\mathcal{W}=1$ next to the soliton core), and presents a strong spin polarization of $\tilde{S}=0.67$, thus pointing towards the non-trivial character of the optically created interface. Since the soliton does not create an infinite potential barrier, the emerging topological edge state in the excitation spectrum is not fully spin polarized as one would expect otherwise. These simulations appeal for further explorations to experimentally demonstrate the emergence of an edge state in the SSH topological gap induced by dissipatively stabilized gap solitons showing high spin polarization.

Outlook

This work provides exciting perspectives to nonlinear topological photonics. Indeed, the driven-dissipative nature of polaritonic systems offers a general way to stabilize novel nonlinear solutions that find no equivalent in conservative systems, to engineer non-Hermitian defects as well as to reshape the potential landscape probed by Bogoliubov excitations and to modify their topology^{53,54}. The control over the imaginary part of the potential could enable the exploration of PT-symmetric phases in nonlinear driven-dissipative systems^{40,55}. These ideas can be extended to more complex non-Hermitian landscapes with chiral symmetry like two-dimensional polariton lattices^{17,43,56,57} or higher-order topological insulators^{58–60}.

Online content

Any methods, additional references, Nature Research reporting summaries, source data, extended data, supplementary information, acknowledgements, peer review information; details of

author contributions and competing interests; and statements of data and code availability are available at <https://doi.org/10.1038/s41567-022-01599-8>.

Received: 18 December 2020; Accepted: 28 January 2022;

Published online: 09 May 2022

References

- Hasan, M. Z. & Kane, C. L. Colloquium: topological insulators. *Rev. Mod. Phys.* **82**, 3045–3067 (2010).
- Qi, X. L. & Zhang, S. C. Topological insulators and superconductors. *Rev. Mod. Phys.* **83**, 1057 (2011).
- Cooper, N. R., Dalibard, J. & Spielman, I. B. Topological bands for ultracold atoms. *Rev. Mod. Phys.* **91**, 015005 (2019).
- Lu, L., Joannopoulos, J. D. & Soljačić, M. Topological photonics. *Nat. Photon.* **8**, 821–829 (2014).
- Ozawa, T. et al. Topological photonics. *Rev. Mod. Phys.* **91**, 015006 (2019).
- Huber, S. D. Topological mechanics. *Nat. Phys.* **12**, 621–623 (2016).
- Peano, V., Brendel, C., Schmidt, M. & Marquardt, F. Topological phases of sound and light. *Phys. Rev. X* **5**, 031011 (2015).
- Klembt, S. et al. Exciton-polariton topological insulator. *Nature* **562**, 552–556 (2018).
- Gianfrate, A. et al. Measurement of the quantum geometric tensor and of the anomalous Hall drift. *Nature* **578**, 381–385 (2020).
- Ozawa, T. & Price, H. M. Topological quantum matter in synthetic dimensions. *Nat. Rev. Phys.* **1**, 349–357 (2019).
- Meier, E. J. et al. Observation of the topological Anderson insulator in disordered atomic wires. *Science* **362**, 929–933 (2018).
- Stützer, S. et al. Photonic topological Anderson insulators. *Nature* **560**, 461–465 (2018).
- Kraus, Y. E., Lahini, Y., Ringel, Z., Verbin, M. & Zilberberg, O. Topological states and adiabatic pumping in quasicrystals. *Phys. Rev. Lett.* **109**, 106402 (2012).
- Serra-Garcia, M. et al. Observation of a phononic quadrupole topological insulator. *Nature* **555**, 342–345 (2018).
- Peterson, C. W., Benalcazar, W. A., Hughes, T. L. & Bahl, G. A quantized microwave quadrupole insulator with topologically protected corner states. *Nature* **555**, 346–350 (2018).
- Smirnova, D., Leykam, D., Chong, Y. & Kivshar, Y. Nonlinear topological photonics. *Appl. Phys. Rev.* **7**, 021306 (2020).
- Bleu, O., Solnyshkov, D. D. & Malpuech, G. Interacting quantum fluid in a polariton Chern insulator. *Phys. Rev. B* **93**, 085438 (2016).
- Hadad, Y., Soric, J. C., Khanikaev, A. B. & Alù, A. Self-induced topological protection in nonlinear circuit arrays. *Nat. Electron.* **1**, 178–182 (2018).
- Maczewsky, L. J. et al. Nonlinearity-induced photonic topological insulator. *Science* **370**, 701–704 (2020).
- Mittal, S., Goldschmidt, E. A. & Hafezi, M. A topological source of quantum light. *Nature* **561**, 502–506 (2018).
- Kruk, S. et al. Nonlinear light generation in topological nanostructures. *Nat. Nanotechnol.* **14**, 126–130 (2019).
- Lumer, Y., Plotnik, Y., Rechtsman, M. C. & Segev, M. Self-localized states in photonic topological insulators. *Phys. Rev. Lett.* **111**, 243905 (2013).
- Solnyshkov, D. D., Bleu, O., Teklu, B. & Malpuech, G. Chirality of topological gap solitons in bosonic dimer chains. *Phys. Rev. Lett.* **118**, 023901 (2017).
- Bisianov, A., Wimmer, M., Peschel, U. & Egorov, O. A. Stability of topologically protected edge states in nonlinear fiber loops. *Phys. Rev. A* **100**, 063830 (2019).
- Mukherjee, S. & Rechtsman, M. C. Observation of Floquet solitons in a topological bandgap. *Science* **368**, 856–859 (2020).
- Guo, M. et al. Weakly nonlinear topological gap solitons in Su–Schrieffer–Heeger photonic lattices. *Opt. Lett.* **45**, 6466–6469 (2020).
- Jürgensen, M., Mukherjee, S. & Rechtsman, M. C. Quantized nonlinear Thouless pumping. *Nature* **596**, 63–67 (2021).
- Jürgensen, M. & Rechtsman, M. C. The Chern number governs soliton motion in nonlinear Thouless pumps. *Phys. Rev. Lett.* **128**, 113901 (2022).
- De Léséleuc, S. et al. Observation of a symmetry-protected topological phase of interacting bosons with Rydberg atoms. *Science* **365**, 775–780 (2019).
- Clark, L. W., Schine, N., Baum, C., Jia, N. & Simon, J. Observation of Laughlin states made of light. *Nature* **582**, 41–45 (2020).
- Bergholtz, E. J., Budich, J. C. & Kunst, F. K. Exceptional topology of non-Hermitian systems. *Rev. Mod. Phys.* **93**, 015005 (2021).
- Solnyshkov, D. D., Nalitov, A. V. & Malpuech, G. Kibble–Zurek mechanism in topologically nontrivial zigzag chains of polariton micropillars. *Phys. Rev. Lett.* **116**, 046402 (2016).
- St-Jean, P. et al. Lasing in topological edge states of a one-dimensional lattice. *Nat. Photon.* **11**, 651–656 (2017).
- Zhao, H. et al. Topological hybrid silicon microlasers. *Nat. Commun.* **9**, 981 (2018).

35. Parto, M. et al. Complex edge-state phase transitions in 1D topological laser arrays. In *Conference on Lasers and Electro-Optics FM2E.5* (Optica Publishing Group, 2018).
36. Bahari, B. et al. Nonreciprocal lasing in topological cavities of arbitrary geometries. *Science* **358**, 636–640 (2017).
37. Bandres, M. A. et al. Topological insulator laser: experiments. *Science* **359**, eaar4005 (2018).
38. Weimann, S. et al. Topologically protected bound states in photonic parity-time-symmetric crystals. *Nat. Mater.* **16**, 433–438 (2017).
39. Xia, S. et al. Nonlinear tuning of PT symmetry and non-Hermitian topological states. *Science* **372**, 72–76 (2021).
40. Konotop, V. V., Yang, J. & Zezyulin, D. A. Nonlinear waves in PT-symmetric systems. *Rev. Mod. Phys.* **88**, 035002 (2016).
41. Jeon, D. H., Reisner, M., Mortessagne, F., Kottos, T. & Kuhl, U. Non-Hermitian CT-symmetric spectral protection of nonlinear defect modes. *Phys. Rev. Lett.* **125**, 113901 (2020).
42. Liu, Y. G. N., Jung, P. S., Parto, M., Christodoulides, D. N. & Khajavikhan, M. Gain-induced topological response via tailored long-range interactions. *Nat. Phys.* **17**, 704–709 (2021).
43. Bardyn, C. E., Karzig, T., Refael, G. & Liew, T. C. Chiral Bogoliubov excitations in nonlinear bosonic systems. *Phys. Rev. B* **93**, 020502 (2016).
44. Su, W. P., Schrieffer, J. R. & Heeger, A. J. Solitons in polyacetylene. *Phys. Rev. Lett.* **42**, 1698–1701 (1979).
45. Tanese, D. et al. Polariton condensation in solitonic gap states in a one-dimensional periodic potential. *Nat. Commun.* **4**, 1749 (2013).
46. Cerda-Méndez, E. A. et al. Exciton-polariton gap solitons in two-dimensional lattices. *Phys. Rev. Lett.* **111**, 146401 (2013).
47. Whittaker, C. E. et al. Effect of photonic spin-orbit coupling on the topological edge modes of a Su-Schrieffer-Heeger chain. *Phys. Rev. B* **99**, 081402 (2019).
48. Carusotto, I. & Ciuti, C. Quantum fluids of light. *Rev. Mod. Phys.* **85**, 299–366 (2013).
49. Delplace, P., Ullmo, D. & Montambaux, G. Zak phase and the existence of edge states in graphene. *Phys. Rev. B* **84**, 195452 (2011).
50. Mangussi, F. et al. Multi-orbital tight binding model for cavity-polariton lattices. *J. Phys.: Condens. Matter* **32**, 315402 (2020).
51. Smirnova, D. A., Smirnov, L. A., Leykam, D. & Kivshar, Y. S. Topological edge states and gap solitons in the nonlinear Dirac model. *Laser & Photonics Rev.* **13**, 1900223 (2019).
52. Castin, Y. Bose-Einstein condensates in atomic gases: simple theoretical results. *Coherent Atomic Matter Waves* 1–136 (Springer, 2001).
53. Diehl, S., Rico, E., Baranov, M. A. & Zoller, P. Topology by dissipation in atomic quantum wires. *Nat. Phys.* **7**, 971–977 (2011).
54. Bardyn, C.-E. et al. Topology by dissipation. *New J. Phys.* **15**, 085001 (2013).
55. Comaron, P., Shahnazaryan, V., Brzezicki, W., Hyart, T. & Matuszewski, M. Non-Hermitian topological end-mode lasing in polariton systems. *Phys. Rev. Research* **2**, 022051 (2020).
56. Kartashov, Y. V. & Skryabin, D. V. Modulational instability and solitary waves in polariton topological insulators. *Optica* **3**, 1228–1236 (2016).
57. Gulevich, D. R., Yudin, D., Skryabin, D. V., Iorsh, I. V. & Shelykh, I. A. Exploring nonlinear topological states of matter with exciton-polaritons: edge solitons in kagome lattice. *Sci. Rep.* **7**, 1780 (2017).
58. Mittal, S. et al. Photonic quadrupole topological phases. *Nat. Photon.* **13**, 692–696 (2019).
59. El Hassan, A. et al. Corner states of light in photonic waveguides. *Nat. Photon.* **13**, 697–700 (2019).
60. Banerjee, R., Mandal, S. & Liew, T. C. H. Coupling between exciton-polariton corner modes through edge states. *Phys. Rev. Lett.* **124**, 063901 (2020).

Publisher's note Springer Nature remains neutral with regard to jurisdictional claims in published maps and institutional affiliations.

© The Author(s), under exclusive licence to Springer Nature Limited 2022

Methods

Sample description. The polariton lattice used in this work is etched out of a planar semiconductor microcavity with a nominal quality factor of $Q \approx 75,000$ grown by molecular-beam epitaxy. The microcavity is composed of a λ GaAs layer embedded between two $\text{Ga}_{0.9}\text{Al}_{0.1}\text{As}/\text{Ga}_{0.05}\text{Al}_{0.95}\text{As}$ distributed Bragg reflectors with 28 (top) and 32 (bottom) pairs. A single 15 nm $\text{In}_{0.05}\text{Ga}_{0.95}\text{As}$ quantum well is inserted at the centre of the cavity, resulting in strong exciton–photon coupling, with an associated 3.2 meV Rabi splitting (measured by probing the polariton dispersion via angularly resolved photoluminescence (Supplementary Section 1)). After the epitaxy, the sample is processed with electron-beam lithography and dry etching into arrays of coupled pillars arranged in an SSH lattice. The exciton–photon detuning, defined as the energy difference between the uncoupled cavity mode at the bottom of the s band and exciton resonance, is of the order of -4.9 meV for all the experiments (Supplementary Section 1). Effective couplings J and J' are of the order $J \approx 0.5$ meV and $J' \approx 0.2$ meV.

Experimental techniques. The sample is held at $T = 4$ K in a closed-cycle cryostat. Non-resonant photoluminescence measurements are realized with a single-mode continuous-wave laser at 780 nm. The excitation spot is elongated (FWHM, ~ 30 μm) by focusing the beam with a cylindrical lens at the back-focal plane of the excitation objective. The emission is collected through a lens with a numerical aperture of 0.55 and imaged on the entrance slit of a spectrometer coupled to a charge-coupled device camera with ~ 30 μeV spectral resolution. Real- and momentum-space photoluminescence images are realized by imaging the sample surface and the Fourier plane of the objective, respectively. A polarizer is used to select the emission polarized along the long axis of the lattice. Experiments with quasi-resonant excitation are realized in transmission geometry, with the excitation (detection) on the epitaxial (substrate) side of the sample and a spot of 3.5 μm FWHM. The optical defect is created by focusing an 825 nm continuous-wave laser onto a 3 μm FWHM spot on the epitaxial side. For the resonant two-spot experiment (each with 3.5 μm FWHM), the phase difference is controlled with a delay line with one of the mirrors mounted on a piezoelectric actuator.

Numerical methods. We use the third-order Adams–Bashforth method for the numerical integration of the nonlinear Gross–Pitaevskii equation with a time step of 10^{-3} ps. CPU-based parallel computing is used to evaluate the kinetic energy term via fast Fourier transform. The numerical grid of $2^9 = 512$ points allows to describe a lattice of 21 dimers with a step of 0.25 μm . Increasing the resolution further or considering a longer chain does not change the results. The ramp-up and ramp-down times are 20 ns, which is a compromise between the required adiabaticity and simulation time. We have checked that increasing the ramp-up time further does not change the results. The parameters were as follows: $m = 3 \times 10^{-5} m_0$ (m_0 is the free electron mass); $\gamma = 70$ μeV ; $g = 5$ μeV μm^{-2} ; pumping spot FWHM, ~ 2.8 μm ; and pumping-frequency detuning with respect to the band edge, ~ 0.2 meV. Other relevant parameters, such as the potential profile, are provided and discussed in the Supplementary Information. Bogoliubov spectra were calculated by linearizing the discretized Gross–Pitaevskii equation around the steady-state solution ψ^s . We use the ansatz $\psi_n = (\psi_n^s + \delta\psi_n) \exp(i\omega t)$ with $\delta\psi_n = \mathbf{u}_n \exp(-i\epsilon t/\hbar) + \mathbf{v}_n^* \exp(i\epsilon^* t/\hbar)$, where ϵ is the complex-valued energy⁶¹ and \mathbf{u} and \mathbf{v} are two component vectors describing the amplitude of the wavefunction of the A and B sites in the n th unit cell. The spectrum is symmetric with respect to the pump energy $\epsilon = 0$ meV, as imposed by particle–hole symmetry.

In the graph shown in Fig. 4d, we display the energy versus position distribution of the $|\mathbf{u}_n|^2$ component that is associated with the creation operator. The squared amplitudes corresponding to the A and B sites of the n th unit cell are associated with site numbers $2n$ and $(2n + 1)$, respectively.

Data availability

Source data are provided with this paper. All other data that support the plots within this paper and other findings of this study are available from the corresponding author upon reasonable request.

References

- Sarchi, D., Carusotto, I., Wouters, M. & Savona, V. Coherent dynamics and parametric instabilities of microcavity polaritons in double-well systems. *Phys. Rev. B* **77**, 125324 (2008).

Acknowledgements

We would like to thank I. Carusotto for fruitful discussions. This work was supported by the Paris Ile-de-France Région in the framework of DIM SIRTEQ (J.B.), the Marie Skłodowska-Curie individual fellowship ToPol (P.St.-J.), the H2020-FETFLAG project PhoQus (820392) (J.B. and A.A.), the QUANTERA project Interpol (ANR-QUAN-0003-05) (J.B.), the French National Research Agency project Quantum Fluids of Light (ANR-16-CE30-0021) (G.M. and J.B.), European Research Council via projects EmergenTopo (865151) (A.A.) and ARQADIA (949730) (S.R.), the French RENATECH network, the French government through the Programme Investissement d'Avenir (I-SITE ULNE/ANR-16-IDEX-0004 ULNE) (G.M. and D.D.S.) and IDEX-ISITE initiative 16-IDEX-0001 (CAP 20-25), managed by the Agence Nationale de la Recherche, the Labex CEMPI (ANR-11-LABX-0007) (A.A.).

Author contributions

N.P. and P.St.-J. performed the experiments and analysed the data. N.P. performed the initial theoretical modelling of the experiments using the tight-binding approach, which led to the discovery of spin-polarized topological solitons. D.D.S. and G.M. provided the theoretical guidance and performed the theoretical calculations in the 1D continuous model. N.P., P.St.-J., D.D.S., G.M., N.C.Z., Q.F., B.R., O.J., A.A., S.R. and J.B. participated in the scientific discussions. N.P., P.St.-J., D.D.S., G.M., A.A., S.R. and J.B. wrote the manuscript. N.C.Z., Q.F. and B.R. contributed to the editing of the manuscript. P.St.-J., S.R., J.B. and A.A. designed the sample. A.L., L.L.G., T.B., A.H. and I.S. fabricated the samples. A.A., S.R. and J.B. supervised the work.

Competing interests

The authors declare no competing interests.

Additional information

Supplementary information The online version contains supplementary material available at <https://doi.org/10.1038/s41567-022-01599-8>.

Correspondence and requests for materials should be addressed to Jacqueline Bloch.

Peer review information *Nature Physics* thanks the anonymous reviewers for their contribution to the peer review of this work.

Reprints and permissions information is available at www.nature.com/reprints.